

# Non-parametric Vignetting Correction for Sparse Spatial Transcriptomics Images

Bovey Y. Rao<sup>1,2</sup>, Alexis M. Peterson<sup>2</sup>, Elena K. Kandror<sup>2</sup>, Stephanie Herrlinger<sup>1,2</sup>, Attila Losonczy<sup>1,2,3</sup>, Liam Paninski<sup>2,4,5,6</sup>, Abbas H. Rizvi<sup>2( $\boxtimes$ )</sup>, and Erdem Varol<sup>2,4,5,6( $\boxtimes$ )</sup>

Department of Neuroscience, Columbia University, New York, NY, USA
Zuckerman Mind Brain Behavior Institute, Columbia University,
New York, NY, USA

abbas.rizvi@columbia.edu

- <sup>3</sup> Kavli Institute for Brain Sciences, Columbia University, New York, NY, USA
  - <sup>4</sup> Department of Statistics, Columbia University, New York, NY, USA
  - <sup>5</sup> Grossman Center for the Statistics of the Mind, Columbia University, New York, NY, USA

**Abstract.** Spatial transcriptomics techniques such as STARmap [15] enable the subcellular detection of RNA transcripts within complex tissue sections. The data from these techniques are impacted by optical microscopy limitations, such as shading or vignetting effects from uneven illumination during image capture. Downstream analysis of these sparse spatially resolved transcripts is dependent upon the correction of these artefacts. This paper introduces a novel non-parametric vignetting correction tool for spatial transcriptomic images, which estimates the illumination field and background using an efficient iterative sliced histogram normalization routine. We show that our method outperforms the stateof-the-art shading correction techniques both in terms of illumination and background field estimation and requires fewer input images to perform the estimation adequately. We further demonstrate an important downstream application of our technique, showing that spatial transcriptomic volumes corrected by our method yield a higher and more uniform gene expression spot-calling in the rodent hippocampus. Python code and a demo file to reproduce our results are provided in the supplementary material and at this github page: https://github.com/BoveyRao/ Non-parametric-vc-for-sparse-st.

**Electronic supplementary material** The online version of this chapter (https://doi.org/10.1007/978-3-030-87237-3\_45) contains supplementary material, which is available to authorized users.

<sup>&</sup>lt;sup>6</sup> Center for Theoretical Neuroscience, Columbia University, New York, NY, USA ev2430@columbia.edu

B. Y. Rao and A. M. Peterson—These authors contributed equally.

<sup>©</sup> Springer Nature Switzerland AG 2021 M. de Bruijne et al. (Eds.): MICCAI 2021, LNCS 12908, pp. 466–475, 2021. https://doi.org/10.1007/978-3-030-87237-3\_45

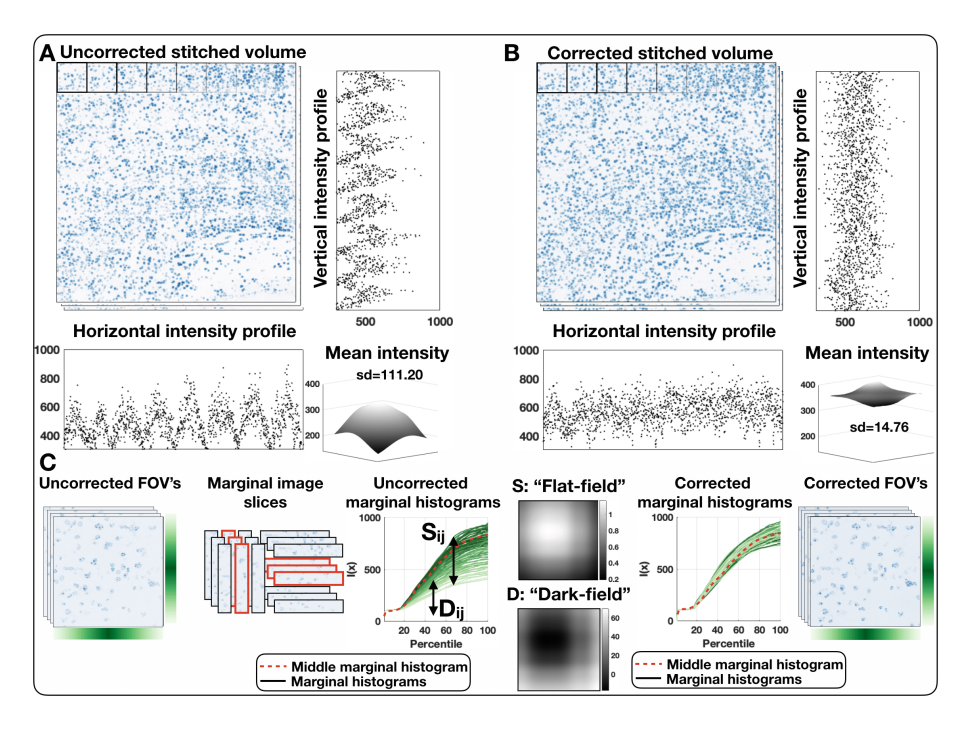


Fig. 1. Overview of the proposed method. A: Vignetting in individual FOVs results in discontinuities in pixel intensities in stitched volumes. B: After applying our proposed technique, the pixel intensities are made uniform across the entire FOV, yielding seamless intensity profiles in stitched volumes. C: Our method estimates the "flat-field" and "dark-field" pixel transformation matrices by iteratively scaling and shifting the histograms of vertical and horizontal strips of all FOVs to match the histograms of "central" strips of the FOVs. The iteratively estimated parameters are then used to derive "flat-field" and "dark-field" matrices. These matrices are then applied to each FOV to ensure that all marginal histograms match closely with the histogram of central regions, ensuring uniformity of pixel intensities throughout all FOVs, countering the effects of vignetting.

#### 1 Introduction

Complex neural representations necessitate experimental and analytical schemes to assess genetically defined cellular populations with spatial resolution. in situ sequencing [6,7] affords the ability to interrogate neural circuits within a histological context but is subject to optical limitations. Uneven illumination fields, optical vignetting, chromatic aberration, and detection noise are inherent to imaging platforms and are a significant obstacle to accurately determine the precise number and location of gene expression in situ.

In addition to a wealth of literature on vignetting correction in natural images [3,17], several techniques have been introduced in recent years for microscopy applications [9–12]. These techniques address non-uniformity in illumination but

underperform when applied to spatial transcriptomic images, given the inherent sparsity. Furthermore, they often require tedious parameter settings to reflect the sparsity of the cell population under view.

In this paper, we posit that if there was no vignetting, aggregated marginal regions of images in a large sample would follow roughly similar intensity distributions due to spatial randomization of objects in view. This property exists regardless of the sparsity of cells in the field of view (FOV), but rather as a consequence of the uniform distribution of objects in arbitrarily imaged tissue sections. Thus, the objective of vignetting correction can be cast as a marginal histogram matching problem [4] aiming to minimize differences in the intensity profiles across different regions of images. To accomplish this, we propose an algorithm that first generates histograms corresponding to horizontal and vertical strips from each FOV. Then, these histograms are iteratively normalized to a reference histogram. The scaling and offsets used to normalize histograms are then used to estimate global transformation terms that reflect the level of spatial amplification needed to uniformize the pixel intensities throughout the slice samples within each FOV.

We extensively evaluate our method in a real rodent spatial transcriptomics dataset and show that it significantly outperforms the state-of-the-art microscopy vignetting correction tools, BASIC [9,10] and CIDRE [12]. Furthermore, we demonstrate an important downstream application of our method by using it to assist in STARmap [15] in situ sequencing imaging-based detection of transcripts within the CA1 region of the mouse hippocampus, demonstrating significantly enhanced detection of transcript specific barcodes [1].

## 2 Method

We first introduce notation. Let  $I \in \mathbf{R}^{N,M}$  denote a  $(N \times M)$  observed spatial transcriptomics FOV such that  $I_{i,j}$  denotes the pixel intensity at the (i,j)th pixel (row/column). We model the observed pixel value as having been transformed from the "true" pixel value,  $I_{i,j}^0$ , through a transformation by a multiplicative "flat-field" matrix,  $S \in \mathbf{R}^{N,M}$  and an additive "dark-field" matrix,  $D \in \mathbf{R}^{N,M}$ :

$$\boldsymbol{I}_{i,j} = \boldsymbol{I}_{i,j}^0 \boldsymbol{S}_{i,j} + \boldsymbol{D}_{i,j} + \epsilon \tag{1}$$

The "flat-field" and "dark-field" matrices model the shading inhomogeneities of foreground and background of the images, respectively [9].

Next, we make an observation that the pixel intensity profiles captured at different rows and columns of many random images would be indicative of potential vignetting artefacts. For example, in a large set of images, if the objects in the bottom right of the image always tend to be darker than the objects in the center of the image, regardless of the objects in view, we can posit that the pixels in the bottom right of the image is subject to lower values of flat-field transformations.

We can quantify pixel intensities using marginal histograms sampled at different rows and columns of images. To estimate the transformation matrices S

and D, we propose to normalize histograms obtained from horizontal and vertical strips of the FOV slices to match the histograms of a "central" reference strip (the robustness is addressed in the Supplementary Materials). We then use the histogram normalization parameters to decode a full spatial estimate of the "flat-field" (S) and "dark-field" (D) matrices. The key idea behind this procedure is that a properly corrected set of images should have indistinguishable histograms in different regions of the image space. See Fig. 1 for an illustration.

In detail, let  $F_{I_{i,:}}^{-1}(q)$  denote the inverse cumulative distribution function (iCDF), evaluating the qth quantile ( $0 \le q \le 1$ ) of the ith row of the all FOVs and  $F_{I_{:,j}}^{-1}(q)$  denote the same thing for the jth column. Furthermore, let  $F_{I_0}^{-1}(q)$  denote the iCDF of a reference strip of the FOV. Note that discretely sampling iCDF is equivalent to generating histograms. Thus, the objective of linearly normalizing the marginally sliced histograms to the reference histogram can be formulated as a linearly parametrized sliced Wasserstein distance [4] minimization problem:

$$\min_{s,d} \int_0^1 ||F_{\boldsymbol{I}_0}^{-1}(q) - F_{\boldsymbol{I}_{i,:}}^{-1}(q)s - d||_2^2 dq \longrightarrow [s \ d]^T = [F_{\boldsymbol{I}_{i,:}}^{-1} \ \mathbf{1}]^{\dagger} F_{\boldsymbol{I}_0}^{-1}$$
 (2)

Here the scalars s and d account for the scaling and additive offsetting of the ith horizontal marginal histogram to match the reference histogram. These terms can be derived by sampling the iCDFs at a discrete number of bins and solving a linear regression problem with the closed form solution:  $[s \ d]^T = [F_{I_{i,:}}^{-1} \ 1]^{\dagger} F_{I_0}^{-1}$ , with  $\dagger$  denoting the Moore–Penrose pseudoinverse. If this operation is repeated for all horizontal slices, we get the vectors  $\mathbf{S}^{\text{horiz}}$ ,  $\mathbf{D}^{\text{horiz}} \in \mathbf{R}^N$ . Next, this procedure can be repeated for all vertical slices to yield  $\mathbf{S}^{\text{vert}}$ ,  $\mathbf{D}^{\text{vert}} \in \mathbf{R}^M$ . If we repeat this procedure, estimating the iterates of  $\mathbf{S}^{t,\text{horiz}}$ ,  $\mathbf{D}^{t,\text{horiz}}$ ,  $\mathbf{S}^{t,\text{vert}}$ ,  $\mathbf{D}^{t,\text{vert}}$  at the tth round whilst simultaneously normalizing the corresponding sliced histograms, we arrive at the following formula to derive an estimate of the "flat-field" and "dark-field" terms:

$$S = \mathbf{1}\mathbf{1}^T \otimes S', \quad D = -D' \otimes S' \tag{3}$$

where  $\oslash$  denotes elementwise division and S' and D' are given by:

$$\mathbf{S'} = \left(\prod_{t} \operatorname{diag}(\mathbf{S}^{t, \operatorname{horiz}}) \mathbf{1} \mathbf{1}^{T} \prod_{t} \operatorname{diag}(\mathbf{S}^{t, \operatorname{vert}})\right)$$
(4)

$$\begin{split} \boldsymbol{D'} &= \sum_{t} \boldsymbol{D}^{t, \text{horiz}} \odot \bigg( \prod_{T-t} \text{diag}(\boldsymbol{S}^{t, \text{horiz}}) \mathbf{1} \mathbf{1}^{T} \prod_{T-t} \text{diag}(\boldsymbol{S}^{t, \text{vert}}) \bigg) + \\ \bigg( \prod_{T-t} \text{diag}(\boldsymbol{S}^{t, \text{horiz}}) \mathbf{1} \mathbf{1}^{T} \prod_{T-t} \text{diag}(\boldsymbol{S}^{t, \text{vert}}) \bigg) \odot \boldsymbol{D}^{t, \text{vert}}. \end{split}$$

Here  $\odot$  denotes row-wise or column-wise multiplication and diag( $\cdot$ ) denotes diagonal matrix. The pseudocode for the routine is provided in Algorithm 1.

Parameter Setting and Histogram Slicing: Note that the procedure to derive sliced iterates of S and D is convergent since each minimization round monotonically reduces the Wasserstein distance to the reference histogram. Importantly, unlike in BASIC [10] where the user has to specify the sparsity penalty, our routine only requires the setting of the level of histogram discretization by a number of bins. Higher number of bins provides more emphasis to middle quantiles of pixel intensities and lower number bins emphasizes the extremes, such as min and max and may provide higher contrast levels in corrected images.

Also, the slicing of marginal histograms does not need to be at a single pixel resolution, and "strips" consisting of multiple contiguous sets of image rows/columns can be utilized and share the same scaling and additive terms. Alternatively, images can be downsampled and sliced along single pixel row/columns to estimate the transformation terms which then can be upsampled to correct full resolution images.

Rank-One Assumption of the Vignetting Field: The estimated "flat-field" and "dark field" are presumed to be rank one by construction. In practice such an assumption is sufficient to capture the convex shaped vignetting field observed in most imaging setups and is due to how we structure the histograms (by rows/columns). Hypothetically, we can normalize arbitrary shapes of histograms, it is possible to sample "checkerboard" patterns of histograms and model any arbitrary rank/shape of vignetting fields.

## Algorithm 1. Iterative sliced histogram normalization

"flat-field"  $\boldsymbol{S}$  and "dark-field"  $\boldsymbol{D}$  estimates, using Eq. (3).

```
Input: Observed set of n FOV's: I = \{I^{u_{(1)},v_{(1)}}, \dots, I^{u_{(n)},v_{(n)}}\} \in \mathbb{R}^{N,M}
 1: for t = 1, \ldots number of iterations do
           Horizontal normalization: Estimate linear regression terms to match ith hor-
           izontal histogram to the reference histogram
           \begin{array}{ll} \mathbf{for} \ i = 1, \dots, N \ \mathbf{do} \\ [\mathbf{S}_i^{(t, \text{horiz})} & \mathbf{D}_i^{(t, \text{horiz})}]^T = \min_{s, d} \int_0^1 ||F_{I_0}^{-1}(q) - F_{I_{i,:}}^{-1}(q)s - d||_2^2 dq \end{array}
 3:
 4:
 5:
           m{I} \longleftarrow m{S}^{(t,	ext{horiz})} m{1}_M^T \odot m{I} + m{D}^{(t,	ext{horiz})} m{1}_M^T for all FOV's
 6:
 7:
           Vertical normalization: Estimate linear regression terms to match jth vertical
           histogram to the reference histogram
           \begin{array}{ll} \mathbf{for} \ j = 1, \dots, M \ \mathbf{do} \\ [\mathbf{S}_j^{(t, \text{vert})} \ \mathbf{D}_i^{(t, \text{vert})}]^T = \min_{s, d} \int_0^1 ||F_{I_0}^{-1}(q) - F_{I_{:,j}}^{-1}(q)s - d||_2^2 dq \end{array}
 8:
 9:
10:
           I \leftarrow \mathbf{1}_N \mathbf{S}^{(t, \text{vert})T} \odot I + \mathbf{1}_N \mathbf{D}^{(t, \text{vert})T} for all FOV's
11:
12: end for
13: return Corrected set of FOV's: \{I^{u_{(1)},v_{(1)}},\ldots,I^{u_{(n)},v_{(n)}}\}\in\mathbf{R}^{N,M}
```

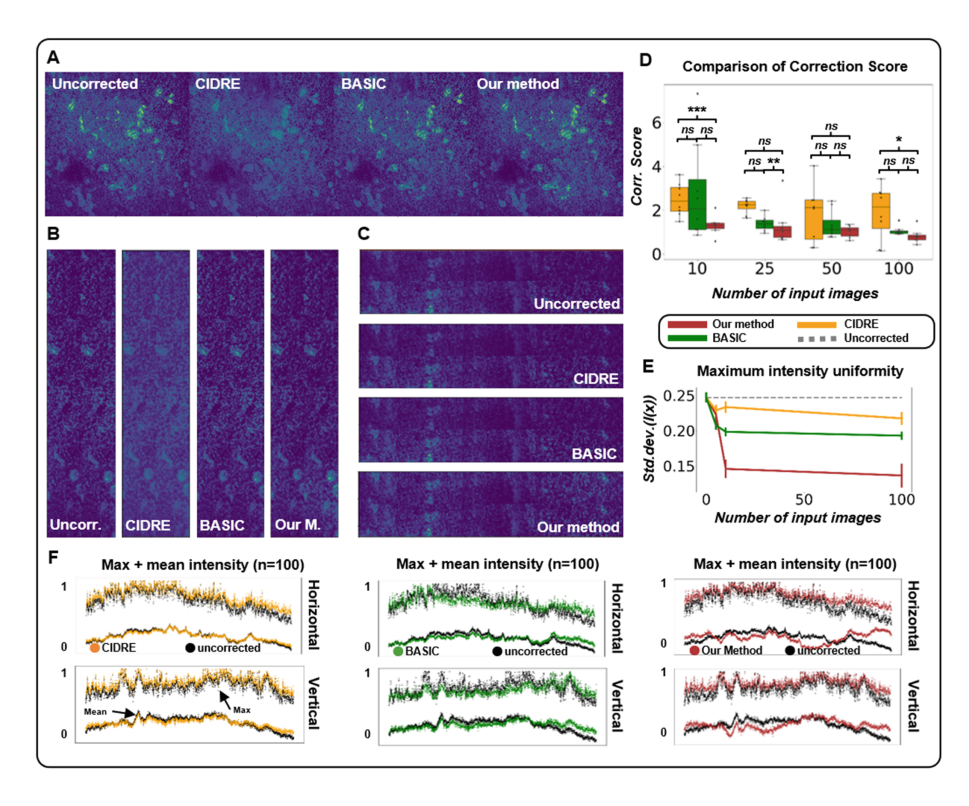


Fig. 2. Vignetting correction evaluation. A: Maximum projection comparison using 3 methods with 100 input images. B: Representative left-right overlap. C: Representative top-bottom overlap. D: Correction scores from 4 left-right and 4 top-bottom overlapping sections. E: Uniformity metric of bootstrapped 0.1% samples of Gaussian filtered maximum projections. F: Vertical and horizontal intensity profiles for max and mean projections compared to that of the raw image. Our method produces flatter images for maximum projections, while having a lower uniformity metric and equal or lower correction scores (\*p < 0.05, \*\*p < 0.01, and \*\*\*p < 0.001 for paired t-test). See Supplementary Materials for additional panels. (Color figure online)

#### 3 Results

Data and Imaging System Description: STARmap based in situ sequencing was performed as previously described [15], utilizing five rounds (of 4 color channels each) of sequencing by ligation to detect 44 transcripts in 20 micron sections of the murine hippocampus. Samples were imaged using an Andor Dragonfly spinning disk confocal microscope [8] utilizing Borealis conditioning for each excitation wavelength and sCMOS based detection of fluorescent output to yield  $2048 \times 2048$  pixel FOV's that cover  $200 \,\mu\text{m} \times 200 \,\mu\text{m}$  area at  $60 \times$  magnification. The depth slices are acquired at increments of  $0.22 \,\mu\text{m}$ . Imaged sequencing rounds were rigidly registered using fast-Fourier-transform-based phase correlation [2]. Our vignetting correction was applied to this field of view with a

downsample factor of 50 and bin size 40, over 5 iterations. After registration, BarDensr [1] was used for spot detection using a detection threshold of 0.95, blur level 2 pixels, tile size of  $250 \times 250$  pixels, and  $5 \times$  downsample level.

**Evaluation Approaches:** For real microscopy images where the ground truth is not available, a thorough evaluation of vignetting correction methods is not trivial. One approach is to compare the estimated flat-field term,  $\hat{\boldsymbol{S}}$ , with a reference flat-field,  $\boldsymbol{S}_{\text{ref}}$ , obtained from a calibration experiment [14]. The key challenge of such a validation is to acquire a reliable reference. As we did not have that option, for one metric, we measured the uniformity of illumination in corrected FOV's by taking the std of pixel intensities in aggregated mean or maximum projected images. This evaluation metric can be formulated as:

Uniformity metric: 
$$u(\mathbf{I}, \sigma) = \sqrt{(1/NM) \sum_{i,j} \left( f(\mathbf{I}, \sigma)_{i,j} - (1/NM) \sum_{i,j} f(\mathbf{I}, \sigma)_{i,j} \right)^2}$$
 (5)

where  $f(\mathbf{I}, \sigma)_{i,j}$  denotes i, jth pixel of the max or mean image that has been Gaussian filtered with a kernel width of  $\sigma$  pixels. We evaluate this metric on z-scored pixel intensities (evaluated across the entire FOV) to keep the scale of this metric normalized and enable comparison across different methods.

In addition to the Uniformity metric we described, we also implemented the correction score ( $I^{corr}$ ) based strategy of measured differences in overlapping regions [9]. This value is formulated as:

Correction score [9]: 
$$\Gamma'(I^{corr}) = \frac{\sum_{x} |I_a^{corr}(x) - I_b^{corr}(x)|}{\sum_{x} |I_a^{meas}(x) - I_b^{meas}(x)|}$$
 (6)

This correction score generates a metric where 0 is a perfect correction, <1 is an improvement from the uncorrected images, 1 is the same as the uncorrected images, and >1 is worse than the uncorrected images.

Vignetting Correction Comparisons with the State-of-the-Art: We compared our method with CIDRE [12] and BASIC [9,10]. CIDRE was the first method to estimate both light and dark fields for image correction [12]. BASIC is another image correction method that estimates the light and dark field and uses sparse and low-rank decomposition to correct vignetting [9,10]. For BASIC and CIDRE, we utilized the respective ImageJ plugins with their default parameters, while using the parameters mentioned above for our method in Python. Our test image stack was from the murine spatial transcriptomic experiment with dimensions of  $2048 \times 2048 \times 191$ . We selected random subsets of 5, 10, 25, 50, and 100 image slices to build correction models for all three methods.

All three methods showed some level of vignetting correction from the uncorrected images (Fig. 2A). We applied the correction score methodology on 8 sets of overlapping regions (4 top-bottom, 4 left-right) (Fig. 2B-C). Our correction score results across all numbers of input images were equal or lower than both

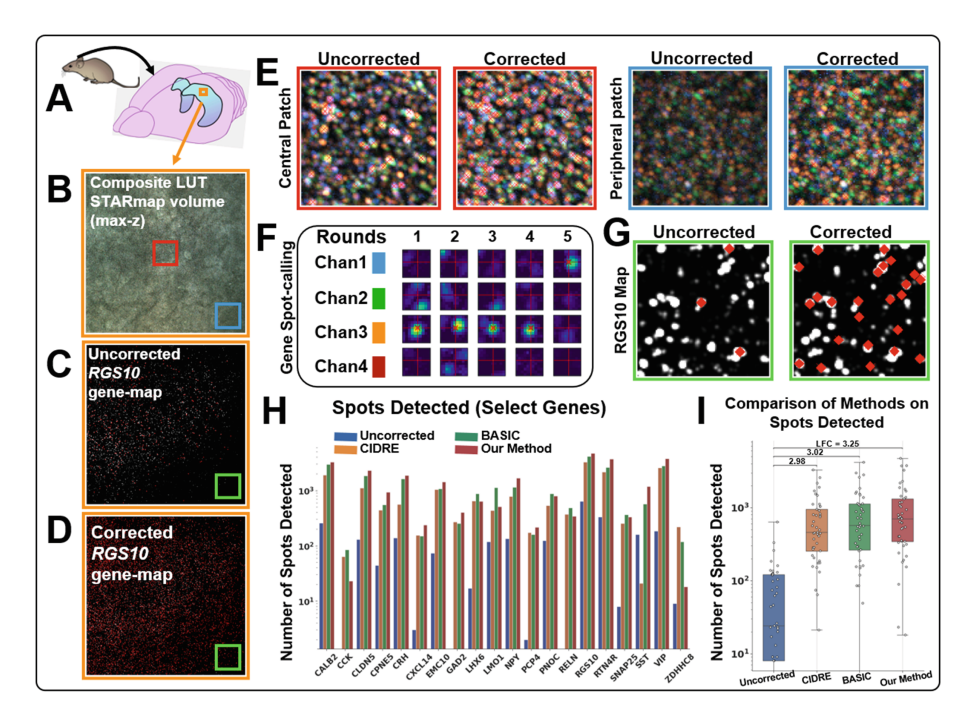


Fig. 3. Vignetting correction improves spot calling and gene detection. A: STARmap based detection of 44 transcripts within CA1. B: Data was rigidly registered and projected across the depth axis. C: Detection of the RGS10 transcript in uncorrected image yields uneven spot calling and uneven localization. D: Vignetting correction enhances spot detection of RGS10. E: Magnified fields of view from central (red) and peripheral (blue) regions. F: RGS10 spot detected using BarDensr following vignetting correction G: RGS10 has a higher rate of detection post vignetting correction (green). H: Absolute gene count for uncorrected (blue) versus vignetting corrected images using CIDRE (orange), BASIC (green), and our method (red). I: Gene spots detected in uncorrected and corrected images with average log fold change (LFC). Our method improves spot detection as compared to CIDRE and BASIC correction methods. (Color figure online)

CIDRE and BASIC (Fig. 2D). We also bootstrapped 0.1% samples of Gaussian filtered pixels and computed the Uniformity metric, where our method had the lowest value (Fig. 2E). We also observed the maximum and mean intensities along the horizontal and vertical axes to provide another qualitative metric for the corrected stack's flatness (Fig. 2F and in the Supplementary Materials). Our vignetting correction method works more effectively on maximum intensities than BASIC and CIDRE with roughly equivalent results for mean intensities.

Gene spot calling techniques like BarDensr [1] utilize thresholding of highintensity pixels across multiple rounds of barcode imaging, so our technique, which corrects higher quantiles such as the maximum projection, is functionally more relevant for such types of downstream analysis. **Downstream Gene Spot Calling Analysis:** We examined the utility of our method towards spot detection, a process critical to *in situ* sequencing. We performed STARmap multiplexed *in situ* sequencing of the mouse CA1 hippocampal region over five rounds, probing 44 distinct transcripts of interest (Fig. 3A). Sample drift was accounted for by rigidly registering [2] spots round-by-round so that the same spot appeared in a constant location across all rounds. Following registration, the data were projected across the depth axis (Z) to create a  $5 \times 4 \times 2048 \times 2048$  (rounds × channels × image area in pixels) matrix as input into BarDensr (Fig. 3B).

We focused on RGS10, an enriched gene in the hippocampus [5]. In the uncorrected image, detection of RGS10 was sparse and nonuniform, with poor spatial localization (Fig. 3C). Vignetting correction using our approach increased spot calls and their spatial distribution (Fig. 3D). It also improved homogeneity and spot visualization when comparing uncorrected and corrected spots in the central region (red) and periphery (blue) (Fig. 3E). An example of an RGS10 spot fitting these criteria is shown in Fig. 3F. The detection rate of RGS10 improved overall after vignetting correction, and is highlighted specifically in the central region (Fig. 3G).

Absolute gene count was quantified in the uncorrected data and data corrected using CIDRE, BASIC, and our method. As compared to uncorrected data, overall transcript detection increased by an order of magnitude. Previously undetected transcripts, such as GAD2, a marker for interneurons [16], were observed. Many markers were enhanced using our method as compared to CIDRE and BASIC (Fig. 3H and Fig. S15). We compared the average log fold change of spots detected using each vignetting corrected method with the uncorrected data, and our method provided the most consistent increase in spot detection (Fig. 3I). Correction of uneven illumination field using our method offers enhanced analysis of transcriptional activation and localization in tissue.

Conclusion: The approach we describe offers a generalized method to contend with uneven illumination fields, resulting in heightened quantification of multiplexed in situ data. Our approach may offer value to time resolved photobleaching, enabling enhanced discrimination of metabolic flux in tissue and address depth based intensity dropoff effects that result from scattering occurring during deep tissue imaging. Although we highlight the application of this algorithm in murine hippocampal tissue, we anticipate it will offer value towards translational applications including spatially resolved transcriptomic studies of cancer and neurodegenerative diseases as well as other imaging modalities such as 2-photon calcium imaging [13].

**Acknowledgements.** BYR, SH, and AL are supported by NIMH 1R01MH124047 and 1R01MH124867; and NINDS 1U19NS104590 and 1U01NS115530. SH also is supported by NIMH 5K00MH121382. AMP, EKK, and AHR are funded from CZF2019-002460 and 1R01MH124047-01. LP, EV are supported by Simons Foundation 543023, NSF 1912194, NSF NeuroNex Award 1707398 and The Gatsby Charitable Foundation GAT3708.

## References

- Chen, S., Loper, J., Chen, X., Zador, T., Paninski, L.: Barcode demixing through non-negative spatial regression (BarDensr). bioRxiv (2020)
- Guizar-Sicairos, M., Thurman, S.T., Fienup, J.R.: Efficient subpixel image registration algorithms. Opt. Lett. 33(2), 156–158 (2008)
- 3. Kim, S.J., Pollefeys, M.: Robust radiometric calibration and vignetting correction. IEEE Trans. Pattern Anal. Mach. Intell. **30**(4), 562–576 (2008)
- 4. Kolouri, S., Zou, Y., Rohde, G.K.: Sliced Wasserstein kernels for probability distributions. In: Proceedings of the IEEE Conference on Computer Vision and Pattern Recognition, pp. 5258–5267 (2016)
- Lee, J.K., Chung, J., Druey, K.M., Tansey, M.G.: Rgs10 exerts a neuroprotective role through the PKA/C-AMP response-element (CREB) pathway in dopaminergic neuron-like cells. J. Neurochem. 122(2), 333–343 (2012)
- Lee, J.H., et al.: Highly multiplexed subcellular RNA sequencing in situ. Science 343(6177), 1360–1363 (2014)
- Mitra, R.D., Shendure, J., Olejnik, J., Church, G.M., et al.: Fluorescent in situ sequencing on polymerase colonies. Anal. Biochem. 320(1), 55–65 (2003)
- 8. Oreopoulos, J., Berman, R., Browne, M.: Spinning-disk confocal microscopy: present technology and future trends. Methods Cell Biol. 123, 153–175 (2014)
- Peng, T., et al.: A basic tool for background and shading correction of optical microscopy images. Nat. Commun. 8(1), 1–7 (2017)
- Peng, T., Wang, L., Bayer, C., Conjeti, S., Baust, M., Navab, N.: Shading correction for whole slide image using low rank and sparse decomposition. In: Golland, P., Hata, N., Barillot, C., Hornegger, J., Howe, R. (eds.) MICCAI 2014. LNCS, vol. 8673, pp. 33–40. Springer, Cham (2014). https://doi.org/10.1007/978-3-319-10404-1\_5
- 11. Piccinini, F., Bevilacqua, A., Smith, K., Horvath, P.: Vignetting and photobleaching correction in automated fluorescence microscopy from an array of overlapping images. In: 2013 IEEE 10th International Symposium on Biomedical Imaging, pp. 464–467. IEEE (2013)
- 12. Smith, K., et al.: CIDRE: an illumination-correction method for optical microscopy. Nat. Methods **12**(5), 404–406 (2015)
- Stosiek, C., Garaschuk, O., Holthoff, K., Konnerth, A.: In vivo two-photon calcium imaging of neuronal networks. Proc. Natl. Acad. Sci. 100(12), 7319–7324 (2003)
- Tomaževič, D., Likar, B., Pernuš, F.: Comparative evaluation of retrospective shading correction methods. J. Microsc. 208(3), 212–223 (2002)
- 15. Wang, X., et al.: Three-dimensional intact-tissue sequencing of single-cell transcriptional states. Science **361**(6400) (2018)
- 16. Zeisel, A., et al.: Cell types in the mouse cortex and hippocampus revealed by single-cell RNA-Seq. Science **347**(6226), 1138–1142 (2015)
- Zheng, Y., Lin, S., Kambhamettu, C., Yu, J., Kang, S.B.: Single-image vignetting correction. IEEE Trans. Pattern Anal. Mach. Intell. 31(12), 2243–2256 (2008)